

Uncertainty-Aware Molecular Dynamics from Bayesian Active Learning for Phase Transformations and Thermal Transport in SiC

Yu Xie^{a,1}, Jonathan Vandermause,^{1,2} Senja Ramakers,^{3,4}

Nakib H. Protik,¹ Anders Johansson,¹ and Boris Kozinsky^{b1,5}

¹*John A. Paulson School of Engineering and Applied Sciences, Harvard University*

²*Department of Physics, Harvard University*

³*Corporate Sector Research and Advance Engineering, Robert Bosch GmbH, Renningen*

⁴*Interdisciplinary Centre for Advanced Materials Simulation, Ruhr-Universität Bochum*

⁵*Robert Bosch LLC, Research and Technology Center*

Abstract

Machine learning interatomic force fields are promising for combining high computational efficiency and accuracy in modeling quantum interactions and simulating atomistic dynamics. Active learning methods have been recently developed to train force fields efficiently and automatically. Among them, Bayesian active learning utilizes principled uncertainty quantification to make data acquisition decisions. In this work, we present a general Bayesian active learning workflow, where the force field is constructed from a sparse Gaussian process regression model based on atomic cluster expansion descriptors. To circumvent the high computational cost of the sparse Gaussian process uncertainty calculation, we formulate a high-performance approximate mapping of the uncertainty and demonstrate a speedup of several orders of magnitude. We demonstrate the autonomous active learning workflow by training a Bayesian force field model for silicon carbide (SiC) polymorphs in only a few days of computer time and show that pressure-induced phase transformations are accurately captured. The resulting model exhibits close agreement with both *ab initio* calculations and experimental measurements, and outperforms existing empirical models on vibrational and thermal properties. The active learning workflow readily generalizes to a wide range of material systems and accelerates their computational understanding.

^a xiey@g.harvard.edu

^b bkoz@seas.harvard.edu

I. INTRODUCTION

Machine learning interatomic force fields have recently emerged as powerful tools in modeling interatomic interactions. They are capable of reaching near-quantum accuracy while being orders of magnitude faster than *ab initio* methods¹⁻⁹.

Recently, efficient active learning schemes have been demonstrated for high-efficiency data collection, where molecular dynamics (MD) is driven by the machine learning force field, and only configurations satisfying certain acquisition criteria^{6,10-15} are computed with accurate but expensive DFT calculations and added to the training set. Among them, the FLARE⁶ framework utilizes principled Gaussian process (GP) uncertainties to construct a Bayesian force field (BFF), a force field equipped with internal uncertainty quantification from Bayesian inference, enabling a fully autonomous active learning workflow.

The cost of prediction of conventional GP models scales linearly with the training set size, making it computationally expensive for large data sets. The sparse Gaussian process (SGP) approach selects a set of representative atomic environments from the entire training set to build an approximate model, which can scale to a larger training data set, but still suffers from the linear scaling of the inference cost with respect to the sparse set size. To address this issue, it was noticed that for the particular structure of the squared exponential 2+3-body kernel, it is possible to map the mean prediction of a trained model onto an equivalent low-dimensional parametric model^{6,16,17} without any loss of accuracy. It was subsequently shown that the evaluation of the variance can also be mapped onto a low-dimensional model, achieving a dramatically accelerated uncertainty-aware BFF¹⁸. While the 2-body and 3-body descriptions used in the previous work^{6,18} approach the computational speed of classical empirical potentials, they are limited in accuracy. To systematically increase the descriptive power of that approach, it is possible to extend the formalism to include higher body order interactions. However, inclusion of e.g. 4-body interactions requires summing contributions of all quadruplets of atoms in each neighborhood, which adds significant computational expense. Therefore, in a more recent work¹⁹ we used the atomic cluster expansion²⁰ to construct local structure descriptors that scale linearly with the number of neighbors, enabling efficient inclusion of higher body order correlations. An inner product kernel is then constructed based on the rotationally invariant ACE descriptors, forming a basis for a sparse Gaussian Process (GP) regression model for energies, forces and stresses.

Crucially, it was shown in general that in the case of inner-product kernels with high dimensional many-body descriptors, the prediction of the mean can also be mapped exactly onto a constant-cost model via reorganization of the summation in the SGP mean calculation¹⁹. This allows for efficient evaluation of the model forces, energies and stresses, but does not address the cost of evaluating uncertainties. In this work, we present a method to map the variance of SGP models with inner product kernels. This advance enables large-scale uncertainty aware MD and overcome the linear scaling issue of SGPs. Building on this approach, we achieve a significant acceleration of the Bayesian active learning (BAL) workflow and integrate it with Large-scale Atomic/Molecular Massively Parallel Simulator (LAMMPS)²¹. Bayesian force fields are implemented within the LAMMPS MD engine, such that both forces and uncertainties for each atomic configuration are quantified at computational cost independent of the training set size.

As a demonstration of the accelerated autonomous workflow, we train an uncertainty-aware many-body BFF for silicon carbide (SiC) on its several polymorphs and phases. SiC is a wide-gap semiconductor with diverse applications ranging from efficient power electronics to nuclear physics and astronomy. With the discovery of a large number of extrasolar planets²², the compositions and processes under extreme conditions have led to a wide range of studies. In particular, SiC has been identified from the adsorption spectroscopy of carbon-rich extrasolar planets^{23,24}, which has motivated numerous experimental and computational studies of its high temperature high pressure behavior. The phase transition of SiC from the zinc blende (3C) to the rock salt (RS) phase is observed at high pressure in experiments²⁵⁻³¹ and *ab initio* calculations³²⁻³⁹. Empirical potentials such as Tersoff^{40,41}, Vashishta^{42,43}, MEAM⁴⁴, and Gao-Weber⁴⁵ have been developed and applied in large-scale simulations for different purposes. However, empirical analytical potentials are limited in descriptive complexity, and hence accuracy, and require intensive human effort to select training configurations and to train. Machine learning approaches have allowed for highly over-parameterized or non-parametric models to be trained on a wide range of structures and phases^{7,46-50}. Recently, neural network potentials were trained for SiC to study dielectric spectra⁵¹ and thermal transport properties⁵², but they do not capture high-pressure phase transitions.

In the present work, we deploy the accelerated autonomous BAL workflow to the high-pressure phase transition of SiC, and demonstrate that the transition process can be captured

by the uncertainty quantification of the BFF. Then the BFF is used to perform large-scale MD simulations, and compute vibrational and thermal transport properties of different phases. The FLARE BFF shows good agreement with ab-initio calculations⁵³ and experimental measurements, and significantly outperforms available empirical potentials in terms of accuracy, while retaining comparable computational efficiency.

II. RESULTS

A. Accelerated Bayesian Active Learning Workflow

Directly using *ab initio* MD to generate a sufficiently diverse training set for machine learning force fields is expensive and time consuming, and may still miss higher-energy configurations important for rare transformation phenomena. Here, we develop an active learning workflow, where MD is instead driven by the much faster surrogate FLARE many-body BFF. During the MD simulation, the model uses its internal uncertainty quantification, deciding to call DFT only when the model encounters atomic configurations with uncertainty above a chosen threshold. Within this framework, a much smaller number of DFT calls are needed, which greatly reduces the training time and increases the efficiency of phase space exploration.

In this work, we extend the formalism of efficient lossless mapping to include uncertainty of ACE-based many-body SGP models. Specifically, we implement mapped SGP variance to enable efficient uncertainty quantification and achieve large-scale MD simulations by interfacing the Bayesian active learning algorithm with LAMMPS. The mappings of the forces and uncertainty overcome the scaling with the training set size of the computational cost of SGP regression, resulting in a significant acceleration of the training process in comparison with using the full SGP¹⁹.

We illustrate our active learning workflow in Fig. 1a. Starting from a SGP model with a small initial training set, we map both prediction mean and variance into quadratic models to obtain an efficient BFF (details are discussed in *Methods*). With the mapped SGP force field, MD simulation runs in LAMMPS with uncertainty associated with the local energy assigned to each atom in a configuration at each time step. The MD simulation is interrupted once there are atoms whose uncertainties are above the threshold. Then DFT is used to

compute energy, forces and stress for the high-uncertainty configurations. The training set is augmented with the newly acquired DFT data, the SGP model is retrained and mapped, and the MD simulation continues with the updated model.

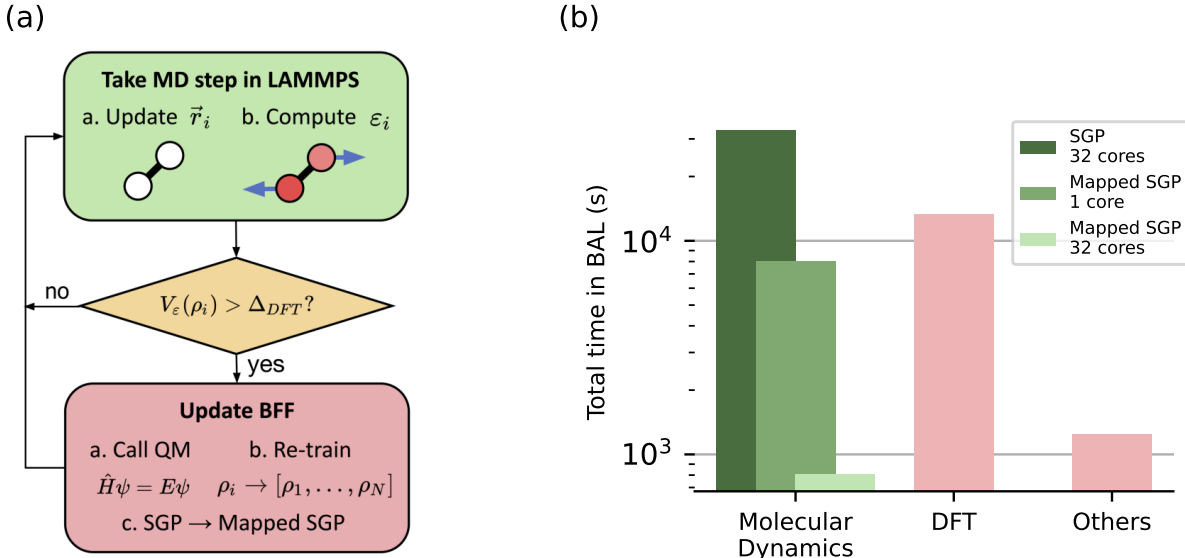


FIG. 1. Workflow and performance. a. Bayesian active learning (BAL) workflow with LAMMPS. It closely follows our previous work¹⁹, with the key addition that the SGP uncertainties are now mapped and therefore much cheaper, and the MD part of the training can be done within LAMMPS. b. Time profiling of the BAL workflow with a system of 72 atoms and 100,000 MD time steps. The SGP BAL workflow collected 14 frames with 72 atoms each, with 10 representative sparse environments selected per frame. The MD is greatly accelerated using mapped forces and uncertainty compared to sparse GP. “Others” includes time consumed outside of MD and DFT, e.g. adding training data to SGP and optimizing hyperparameters.

To illustrate the acceleration of active learning workflow with mapped forces and variance compared to that with the SGP model, we deploy a single active learning run of bulk 4H-SiC system and show the performance of each part of the workflow in Fig. 1b. If the model is not mapped, the computational cost of MD with the SGP dominates the BAL procedure. When the mapped force field and variances are used, the computational cost is significantly reduced. The FLARE BFF achieves 0.76 ms·CPU/step/atom in LAMMPS MD, which includes uncertainty quantification, and is comparable in speed to empirical interatomic potentials such as ReaxFF⁵⁴. With mapped uncertainties, the DFT calculations become

the dominant part from Fig. 1b, i.e. the computational time for BAL is determined by the number of DFT calls. We also note that the SGP model used for timing here has a small training set of 14 frames, and the computational cost of prediction grows linearly with sparse set size. It is worth emphasizing that after mapping, the prediction of model forces, energies, and stresses, and their variances is independent of the sparse set size. Therefore, the speedup versus the SGP model is more pronounced as more training data are collected and sparse representatives are selected.

B. Bayesian Force Field for SiC High Pressure Phase Transition

In this work, we demonstrate the accelerated BAL procedure by training a mapped uncertainty-aware Bayesian force field to describe the phase transition of SiC at high pressure. We set up compressive and decompressive MD simulations at temperatures of 300 K and 2000 K for on-the-fly training simultaneously, where each SGP model is initialized with an empty training set. The parameters set for the on-the-fly training workflow is in the Supplementary Table 1, and the complete training set information is in the Supplementary Table 2.

The compressive MD starts with the 2H, 4H, 6H, and 3C polytypes that are stable at low pressure, and the pressure is increased by 30 GPa every 50 ps. The decompressive MD starts with the RS phase at 200 GPa, and the pressure is decreased by 20 GPa every 50 ps. The training data are collected by the BAL workflow shown in Fig. 1. Fig. 2a shows the system volume and relative uncertainty, i.e. the ratio between the uncertainty of the current frame and the average uncertainty of the training data set (see details in Supplementary Method 1⁵⁵). In the compressive (decompressive) MD, when the transition happens, the volume decreases (increases) rapidly and the uncertainty spikes, since the model has never seen the transition state or the RS (3C) phase before. The post-transition high-pressure structure of the compression run has 6-fold (4-fold) coordination corresponding to the RS (3C) phase, and the transition is observed at 300 GPa (0 GPa) at room temperature. The difference of the transition pressures between the compressive and decompressive simulations is caused by nucleation-driven hysteresis. After the on-the-fly training is done, the training data from compressive and decompressive MD are combined to train a master force field for SiC, such that different phases at different pressures are covered by our force field. In Supplementary

Figure 2 and Supplementary Table 3⁵⁵, we demonstrate the accuracy of our force field on cohesive energy and elastic constants in comparison with DFT.

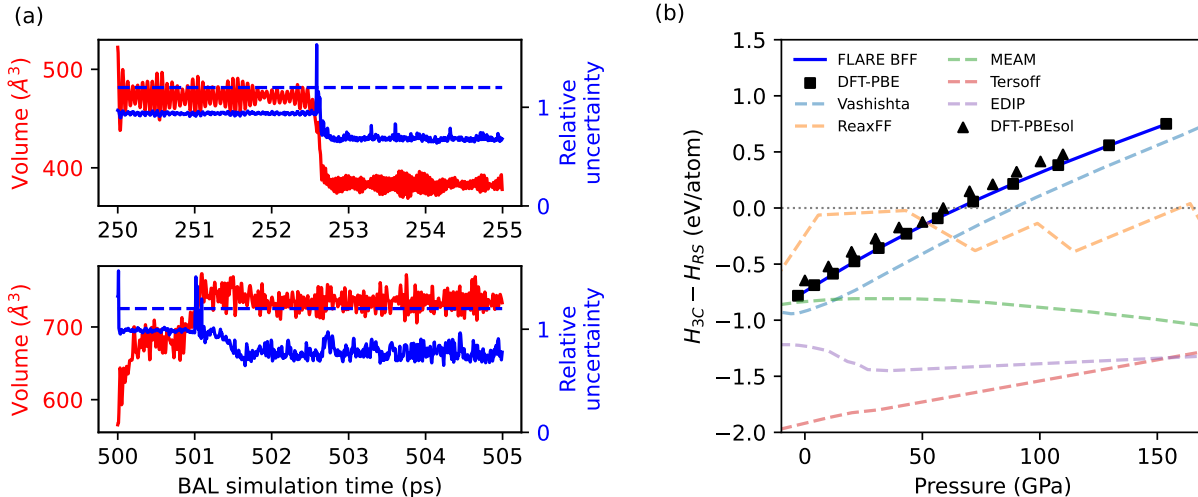


FIG. 2. Phase transition simulation with FLARE BFF and enthalpy calculations. a. A 5 ps segment of the whole training trajectory where the 3C-RS phase transition is captured during the compressive (decompressive) on-the-fly active learning, the volume decreases (increases), and the model uncertainty spikes in the transition state. The uncertainty threshold is shown as the blue dashed line. DFT is called, and new training data is added to the model when the relative uncertainty exceeds the threshold. b. Enthalpy difference predictions from DFT (PBE, PBEsol³⁴), FLARE BFF and existing empirical potentials^{40,42,44,54,56} at pressures from 0 to 150 GPa. The crossing with the dotted zero line gives the transition pressure predicted by enthalpy.

Using the mapped master force field, the phase transition pressure (at zero temperature) can be obtained from the enthalpy $H = E_{\text{total}} + PV$ of the different phases. At low pressure, the RS phase has higher enthalpy than 3C. With the pressure increased above 65 GPa, the enthalpy of RS phase becomes lower than 3C. As shown in Fig.2, empirical potentials such as ReaxFF⁵⁴, MEAM⁴⁴, Tersoff⁴⁰ and EDIP⁵⁶ produce qualitatively incorrect enthalpy curves, likely because they are trained only at low pressures. The Vashishta potential is the only one trained on the high pressure 3C-RS phase transition⁴² and presents a consistent scaling of enthalpy with pressures qualitatively, but it significantly overestimates the transition pressure at 90 GPa compared to DFT. FLARE BFF achieves a good agreement with the *ab initio* (DFT-PBE) enthalpy predictions, with both methods yielding 65 GPa. We note that our PBE value is consistent with previous first-principles calculations such as 66.6(LDA)³²

and 58(PBEsol)³⁴.

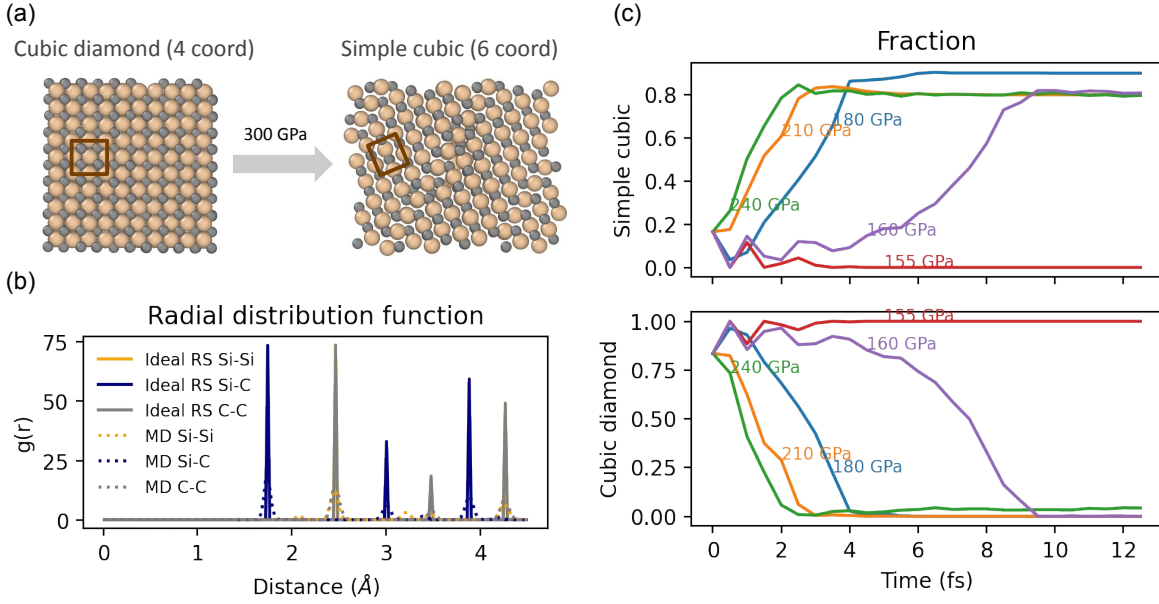


FIG. 3. Large-scale simulation of phase transition and analysis. a. Large-scale MD with 1000 atoms for the 3C-RS phase transition after the training of FLARE BFF is finished. The transition is observed at 300 GPa at room temperature in MD. b. The radial distribution function of the final structure after transition in the MD, compared with the perfect RS crystal lattice, indicating the final configuration is in the RS phase. c. The fraction of simple cubic (RS) and cubic diamond (3C, zinc-blende) atomic environments from the phase boundary evolution at different pressures.

Next we run a large-scale MD simulation with 1000 atoms for 500 ps at the temperature of 300 K. The NPT ensemble is used, and the pressure is increased by 30 GPa every 50 ps. At 300 GPa, the phase transition is observed from 4-fold coordination to 6-fold, as shown in Fig.3b. The final 6-fold coordinated structure has radial distribution function as shown in Fig.3c. The highest C-C, C-Si, Si-Si peaks match the perfect RS structure, confirming that the final structure is in the rock salt phase.

As in the smaller training simulations, the nucleation-controlled hysteresis caused the transition pressure (300 GPa) to be much higher than in experimental measurements (50-150 GPa)^{25,26,28}. To eliminate the nucleation barrier, we start our simulation with a configuration where the 3C and RS phases coexist, separated by a phase boundary, and evolve differently as a function of pressures. It is worth noting that such large scale two-phase simulations

are enabled by the efficient force field and would not be possible to perform with DFT. To recognize simple cubic (RS) and cubic diamond (3C, zinc-blende) environments, we use polyhedral template matching⁵⁷ in OVITO⁵⁸. The time evolution of the fractions of simple cubic and cubic diamond atomic environments is shown in Fig. 3c. The phase boundary evolves quickly within 10 fs. When pressure is greater than 160 GPa, the phase boundary evolves to RS phase, while below 155 GPa it evolves to 3C phase, which indicates the phase transition pressure is located between 155-160 GPa at the temperature of 300 K.

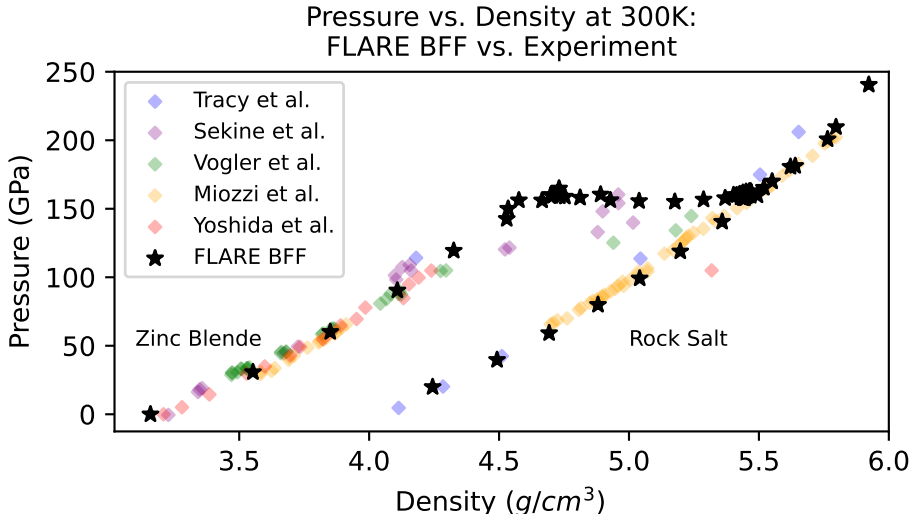


FIG. 4. The density-pressure relation from experimental measurements²⁵⁻²⁹ and MD simulations from FLARE BFF. Zinc blende and rock salt phases correspond to two different lines of equation of state. Our FLARE BFF shows close agreement with experiments.

A number of experiments have measured the density-pressure relations of zinc blende (3C) and rock salt at room temperature²⁵⁻²⁹. As shown in Fig. 4, the equation of state shows two parallel density-pressure curves, where the one with lower density is associated with the zinc-blende phase, and the other one with the rock salt phase. The pressures and corresponding densities at room temperature are extracted from the MD trajectories, and the equation of state is plotted to compare with the experimental measurements. FLARE BFF accurately agrees with the experimental measurements for both phases. For the transition state, there are not many experimental data points available, and the measurements can be affected by the quality of the sample, but the FLARE BFF still shows good agreement with the measured data points.

C. Vibrational and Thermal Transport Properties

To validate that the FLARE BFF gives accurate predictions of thermal properties, we investigate the phonon dispersions and thermal conductivities of the different polytypes and phases of SiC. The phonon dispersions are computed using Phonopy⁵⁹. As shown in Fig. 5, FLARE BFF produces phonon dispersions in close agreement with both DFT and experiments^{60–63} for both the low pressure polytypes and the high pressure rock salt phase at 200 GPa. While in the optical branches the FLARE BFF prediction shows minor discrepancies with DFT at the highest frequencies, the phonon density of states (DOS) presents good agreement. In particular, FLARE BFF captures the peak at 23 THz corresponding to a number of degenerate optical branches. In Supplementary Figure 3, we show that the optical branches can be improved by increasing the cutoff of BFF. Existing empirical potentials are much less accurate than FLARE BFF by comparing the phonon DOS in Fig. 5. We note that the SiC crystals are polarized by atomic displacements and the generated macroscopic field induces an LO-TO splitting near Γ point. The contribution from the polarization should be included through non-analytical correction (NAC)^{59,64}, and the first principle calculation with NAC is discussed in Ref.⁶⁵. However, since FLARE BFF model does not contain charges and polarization, the NAC term is not considered. Thus, our comparison is made between the FLARE BFF and DFT without NAC. The lack of NAC accounts for the disagreement in the high frequencies of the optical bands of 2H DFT phonon (Fig. 5) with experimental measurements near Γ point.

Having confirmed the accuracy of the 2nd order force constants by the phonon dispersion calculations, we then compute the thermal conductivity within the Boltzmann transport equation (BTE) formalism. The 2nd and 3rd order force constants are computed using the Phono3py⁶⁶ code, and then used in the Phoebe⁶⁷ transport code to evaluate thermal conductivity with the iterative BTE solver⁶⁸. In Supplementary Figure 4⁵⁵, we verify that the exclusion of the non-analytic correction does not have a significant effect on the thermal conductivity values. Fig. 5 presents the thermal conductivities of the zinc blende phase at 0 GPa and the rock salt phase at 200 GPa as a function of temperature. The FLARE BFF results are in good agreement with the DFT-derived thermal conductivity for both zinc blende and rock salt phases. The thermal conductivity of zinc blende phase computed from DFT and FLARE BFF is also in good agreement with experimental measurements^{69–72}.

For the high-pressure rock salt phase, the thermal conductivity has not been previously computed or measured to the best of our knowledge. Therefore, our calculation provides a prediction that awaits experimental verification in the future.

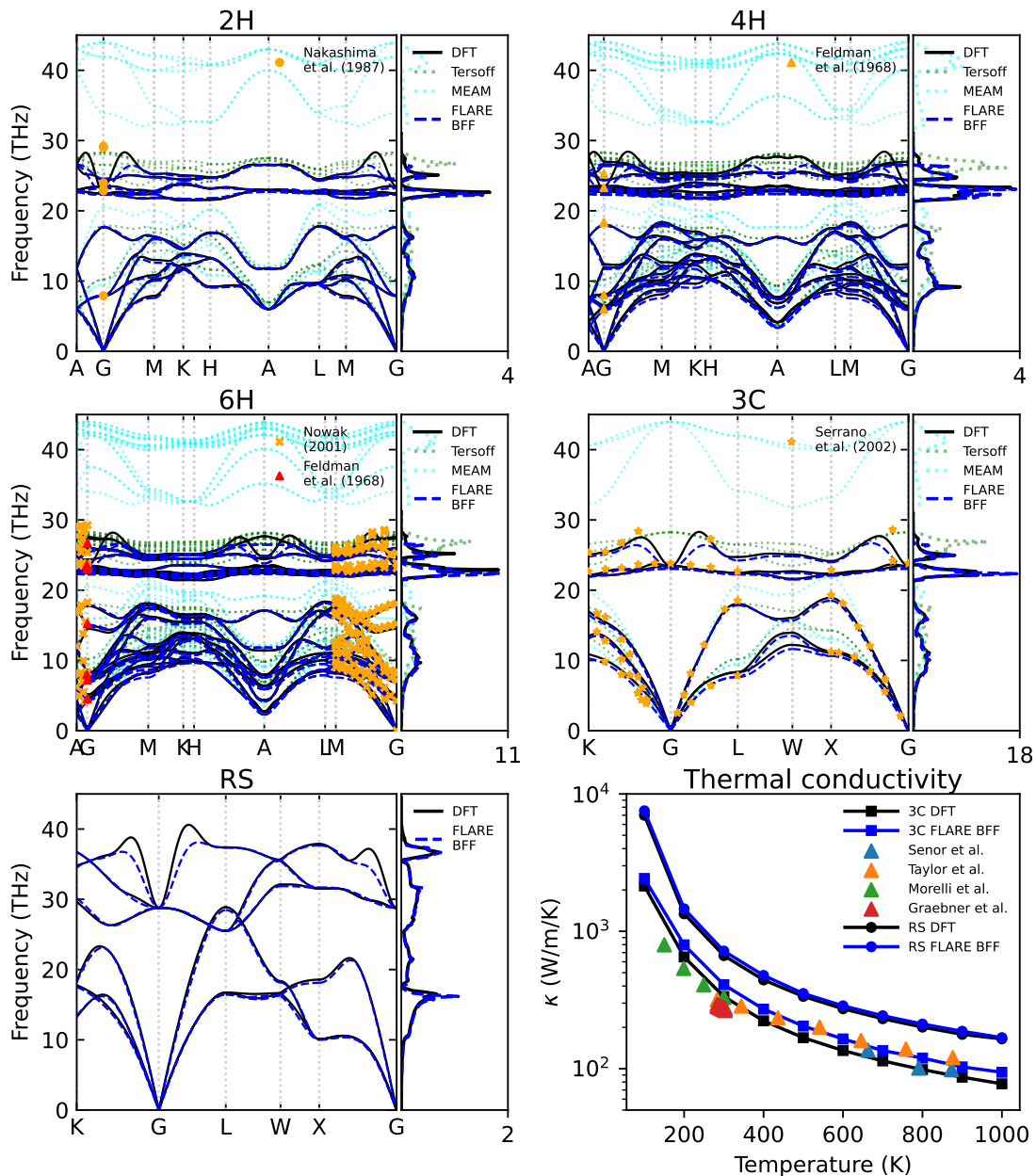


FIG. 5. Phonon dispersions and phonon density of states of different polytypes from experimental measurements^{60–63}, FLARE BFF and DFT calculations. Lower right: Thermal conductivity of 3C-SiC at 0 GPa and RS phase at 200 GPa with temperatures from 100 to 1000 K, from DFT and FLARE BFF calculations, and the experimental measurements^{69–72} are for 3C-SiC.

III. DISCUSSION

In this work we develop a BFF that maps both the mean predictions and uncertainties of SGP models for many-body interatomic force fields. The mapping procedure overcomes the linear scaling issue of SGPs and results in near-quantum accuracy, while retaining computational cost comparable to empirical interatomic potentials such as ReaxFF. The efficient uncertainty-aware BFF model forms the basis for the construction of an accelerated autonomous BAL workflow that is coupled with the LAMMPS MD engine and enables large-scale parallel MD simulations. The key improvement with respect to previous methods is the ability of the many-body model to efficiently calculate forces and uncertainties at comparable computational cost.

As a demonstration of the ability of this method to capture and learn subtle interactions driving phase transformations on-the-fly, we use the BAL workflow to train a BFF for SiC on several common polytypes and phases. The zinc-blende to rock-salt transition is captured in both the active learning and the large-scale simulation, facilitated by the model uncertainty. FLARE BFF is shown to have good agreement with DFT for the enthalpy prediction in a wide range of pressure values. The BFF model is readily employed to perform a large-scale MD of the phase boundary evolution, which allows for reliable identification of the transition pressure at room temperature to be located at 155-160 GPa. The density-pressure relation predicted by FLARE BFF agrees very well with experimental measurements. We also find close agreement for phonon dispersions and thermal conductivities of several SiC phases, as compared with DFT calculations and experiments, outperforming existing empirical potentials.

The high-performance implementation of BFFs, combining accuracy with autonomous uncertainty-driven active learning, opens numerous possibilities to explicitly study dynamics and microscopic mechanisms of phase transformations and non-equilibrium properties such as thermal and ionic transport. The presented unified approach can be extended to a wide range of complex systems and phenomena, where interatomic interactions are difficult to capture with classical approaches while time- and length-scales are out of reach of first-principles computational methods. Uncertainty quantification in MD simulations allows for systematic monitoring of the model confidence and detection of rare and unanticipated phenomena, such as reactions or nucleation of phases. Such events are statistically unlikely

to occur in smaller simulations and become increasingly likely and relevant as the simulation sizes increase, as may be needed to study complex and heterogeneous materials systems.

IV. METHODS

In this section, we use bold letters such as $\boldsymbol{\alpha}$ and $\boldsymbol{\Lambda}$ to denote a vector or a matrix, and use indices such as α_i and Λ_{ij} to denote the components of the vector and matrix respectively. In addition, we use F to represent all the collected configurations with all atomic environments (the “full” data set), and use S for a subset atomic environments selected from those configurations (the “sparse” data set).

A. Gaussian Process Regression

The local atomic environment ρ_i of an atom i consists of all the neighbor atoms within a cutoff radius, and is associated with a label y_i that can be the force \mathbf{F}_i on atom i or a local energy ε_i . The local energy labels are usually not available in practice, but total energies, stresses and atomic forces are. A kernel function $k(\rho_i, \rho_j)$ quantifies the similarity between two atomic environments, which is also the covariance between local energies. Gaussian process regression (GP) assumes a Gaussian joint distribution of all the training data $\{(\rho_i, y_i)\}$ and test data (ρ, y) . The posterior distribution for test data is also Gaussian with the mean and variance

$$\varepsilon(\rho) = \mathbf{k}_{\varepsilon F}(\mathbf{K}_{FF} + \boldsymbol{\Lambda})^{-1}\mathbf{y} \quad (1)$$

$$V(\rho) = k_{\varepsilon\varepsilon} - \mathbf{k}_{\varepsilon F}(\mathbf{K}_{FF} + \boldsymbol{\Lambda})^{-1}\mathbf{k}_{F\varepsilon} \quad (2)$$

Here, ε is the local energy of ρ , $\mathbf{k}_{\varepsilon F}$ is the kernel vector describing covariances between the test data and all the training data, with element $k(\rho, \rho_i)$, $k_{\varepsilon\varepsilon} = k(\rho, \rho)$ is the kernel between test data ρ and itself, \mathbf{K}_{FF} is the kernel matrix with element $k(\rho_i, \rho_j)$, $\boldsymbol{\Lambda}$ is a diagonal matrix describing noise, and \mathbf{y} is the vector of all training labels.

Since the full GP evaluates the kernel between all configurations in the whole training set, it becomes computationally inefficient for large data sets. A sparse approximation is needed such that the computational cost can be reduced while keeping the information as complete as possible. Following our recent work¹⁹ we consider the mean prediction from Deterministic

Training Conditional (DTC) Approximation⁷³, and the variance on local energies

$$\varepsilon(\rho) = \mathbf{k}_{\varepsilon S}(\mathbf{K}_{SF}\mathbf{\Lambda}^{-1}\mathbf{K}_{FS} + \mathbf{K}_{SS})^{-1}\mathbf{K}_{SF}\mathbf{y} \quad (3)$$

$$V(\rho) = k_{\varepsilon\varepsilon} - \mathbf{k}_{\varepsilon S}\mathbf{K}_{SS}^{-1}\mathbf{k}_{S\varepsilon} \quad (4)$$

where the $\mathbf{k}_{\varepsilon S}$ is the kernel vector between the test data ρ and the sparse training set S , \mathbf{K}_{SF} is the kernel matrix between the sparse subset S and the complete training set F , and \mathbf{K}_{SS} is the kernel matrix between S and itself. The energy, forces and stress tensor of a test configuration are given by the mean prediction, and their corresponding uncertainties are given by the square root of the predictive variance.

B. ACE Descriptors with Inner Product Kernel

In the FLARE SGP formalism¹⁹ we use the atomic cluster expansion²⁰ (ACE) descriptors to represent the features of a local environment. The total energy is constructed from atomic clusters, represented by the expansion coefficients of an atomic density function using spherical harmonics. We refer the readers to Ref.^{19,20} for more details. To build up the SGP model for interatomic Bayesian force field, or BFF, we use the inner product kernel defined as

$$k(\rho_1, \rho_2) = \sigma^2 \left(\frac{\mathbf{d}_1 \cdot \mathbf{d}_2}{d_1 d_2} \right)^\xi \quad (5)$$

where \mathbf{d}_1 and \mathbf{d}_2 are ACE descriptors of environments ρ_1 and ρ_2 , σ is the signal variance which is optimized by maximizing the log likelihood of SGP, and ξ is the power of the inner product kernel which is selected a priori. We also normalize the kernel by the L2 norm of the descriptors. For simplicity of notations and without loss of generality, we ignore the normalization and only showcase the kernel without derivative associated with energy.

With inner product kernels, a highly efficient but lossless approximation is available via reorganization of the summation in the mathematical expression¹⁹. Defining $\boldsymbol{\alpha} := (\mathbf{K}_{SF}\mathbf{\Lambda}^{-1}\mathbf{K}_{FS} + \mathbf{K}_{SS})^{-1}\mathbf{K}_{SF}\mathbf{y}$ and $\tilde{\mathbf{d}}_i = \mathbf{d}_i/d_i$, the mean prediction of test data ρ_i (Eq.3)

from sparse training set $S = \{\rho_s\}$ can be written as¹⁹

$$\begin{aligned}
\varepsilon(\rho_i) &= \sigma^2 \sum_t (\tilde{\mathbf{d}}_i \cdot \tilde{\mathbf{d}}_t)^\xi \alpha_t \\
&= \sigma^2 \sum_{t, m_1, \dots, m_\xi} \tilde{d}_{im_1} \tilde{d}_{tm_1} \cdots \tilde{d}_{im_\xi} \tilde{d}_{tm_\xi} \alpha_t \\
&= \sigma^2 \sum_{m_1, \dots, m_\xi} \tilde{d}_{im_1} \cdots \tilde{d}_{im_\xi} \left(\sum_t \tilde{d}_{tm_1} \cdots \tilde{d}_{tm_\xi} \alpha_t \right) \\
&= \sum_{m_1, \dots, m_\xi} \tilde{d}_{im_1} \cdots \tilde{d}_{im_\xi} \beta_{m_1, \dots, m_\xi},
\end{aligned} \tag{6}$$

The β tensor can be computed from the training data descriptors. Thus, we can store the β tensor, and during the prediction we directly evaluate Eq. 6 without the need to sum over all training data t .

Crucially, the variance Eq. 4 has the similar reorganization as the mean prediction of Eq. 6

$$V(\rho_i) = \sigma^2 (\tilde{\mathbf{d}}_i \cdot \tilde{\mathbf{d}}_i)^\xi - \sigma^4 \sum_{s, t} (\tilde{\mathbf{d}}_i \cdot \tilde{\mathbf{d}}_s)^\xi (K_{SS}^{-1})_{st} (\tilde{\mathbf{d}}_t \cdot \tilde{\mathbf{d}}_i)^\xi \tag{7}$$

$$= \sum_{\substack{m_1, \dots, m_\xi \\ n_1, \dots, n_\xi}} (\tilde{d}_{im_1} \cdots \tilde{d}_{im_\xi}) \gamma_{n_1, \dots, n_\xi}^{m_1, \dots, m_\xi} (\tilde{d}_{in_1} \cdots \tilde{d}_{in_\xi}) \tag{8}$$

where γ is a tensor that can be calculated and stored once the training data is collected, and used in inference without explicit summation over training data i .

The reorganization indicates that the SGP regression with inner product kernel essentially gives a polynomial model of the descriptors. Denote n_d as the descriptor dimension. The reorganized mean prediction has both the β size and the computational cost as $O(n_d^\xi)$. While the reorganized variance prediction has both the γ size and the computational cost as $O(n_d^{2\xi})$. By the reorganization, both the mean and variance predictions become independent of the training set and get rid of the linear scaling with respect to training size. Here, we choose $\xi = 2$ for the mean prediction, because 1) it is shown¹⁹ that $\xi = 2$ has a significant improvement of likelihood compared to $\xi = 1$, while the improvement of $\xi > 2$ is marginal; and 2) higher order requires a much larger memory for β tensor, and the evaluation of Eq.6 is much costlier than $\xi = 2$.

From Eq.8 we see that the variance has twice the polynomial degree of that for the mean prediction. For example, when $\xi = 2$, the mean prediction is a quadratic model while the

variance is a quartic model of descriptors. For computational efficiency, in this work we use $V_{\xi=1}$ for variance prediction. $V_{\xi=1}$ is not the exact variance of our mean prediction $\varepsilon_{\xi=2}$, but an approximation using the same hyperparameters as $V_{\xi=2}$. It has a strong correlation with the exact variance $V_{\xi=2}$ as shown in Supplementary Figure 1⁵⁵. Especially, the correlation coefficients between $V_{\xi=1}$ and higher powers are close to 1.0, the perfect linear relation, even with a training size of 200 frames. This indicates that uncertainty quantification with $V_{\xi=1}$ is able to recognize discrepancies between different configurations as well as $V_{\xi=2}$. Specifically, atomic environments with higher $V_{\xi=2}$ uncertainties will also be assigned higher $V_{\xi=1}$ uncertainties than others. It is then justified that $V_{\xi=1}$ can be used as a strongly correlated but much cheaper approximation of $V_{\xi=2}$.

To summarize, we use $\varepsilon_{\xi=2}$ and $V_{\xi=1}$ for mean and variance predictions respectively, where both are quadratic models with respect to the descriptors. During the on-the-fly active learning, every time the training set is updated by the new DFT data, the β and γ matrices are computed from training data descriptors and stored as coefficient files. In LAMMPS MD, the quadratic models are evaluated to make predictions for energy, forces, stress and uncertainty of the configurations.

V. DATA AVAILABILITY

The scripts and data are available in Zenodo: <https://doi.org/10.5281/zenodo.5797177>.

VI. CODE AVAILABILITY

The code for FLARE Bayesian force field and Bayesian active learning is available at <https://github.com/mir-group/flare>.

VII. ACKNOWLEDGEMENT

We thank Lixin Sun, Thomas Eckl, Matous Mrovec, Thomas Hammerschmidt and Ralf Drautz for helpful discussions on the construction of the force field and properties of SiC. We thank Jenny Coulter and Andrea Cepellotti for the helpful instructions on thermal

conductivity calculation using Phono3py and Phoebe. We thank Jenny Hoffman, Sushmita Bhattacharya and Kristina Jacobsson for constructive suggestions on the manuscript. YX was supported from the US Department of Energy (DOE), Office of Science, Office of Basic Energy Sciences (BES) under Award No. DE-SC0020128. JV was supported by the National Science Foundation award number 2003725. AJ was supported by the Aker scholarship. BK was supported by the National Science Foundation through the Harvard University Materials Research Science and Engineering Center under award number DMR-2011754 and Robert Bosch LLC. Computational resources were provided by the FAS Division of Science Research Computing Group at Harvard University.

VIII. AUTHOR CONTRIBUTIONS

J.V., Y.X. and A.J. developed the FLARE code, the corresponding LAMMPS pair styles and compute commands. Y.X. implemented the on-the-fly training workflow coupled with LAMMPS. Y.X. performed the on-the-fly training and MD simulation of SiC. S.R. performed DFT calculations of SiC polymorphs. Y.X. computed the thermal conductivity of SiC with the contribution of N.H.P.. B.K. conceived the application and supervised the work. Y.X. and B.K. wrote the manuscript. All authors contributed to manuscript preparation.

IX. COMPETING INTERESTS

The authors declare no competing financial or non-financial interests.

-
- ¹ Jörg Behler and Michele Parrinello. Generalized neural-network representation of high-dimensional potential-energy surfaces. Phys. Rev. Lett., 98(14):146401, 2007.
 - ² Alexander V Shapeev. Moment tensor potentials: A class of systematically improvable interatomic potentials. Multiscale Model. Simul., 14(3):1153–1173, 2016.
 - ³ Aidan Patrick Thompson, Laura Painton Swiler, Christian Robert Trott, Stephen Martin Foiles, and Garritt J. Tucker. Snap: Automated generation of quantum-accurate interatomic potentials. J. Comput. Phys., 9 2014.

- ⁴ Kristof Schütt, Pieter-Jan Kindermans, Huziel Enoc Saucedo Felix, Stefan Chmiela, Alexandre Tkatchenko, and Klaus-Robert Müller. Schnet: A continuous-filter convolutional neural network for modeling quantum interactions. In *Adv. Neural Inf. Process. Syst.*, pages 991–1001, 2017.
- ⁵ Albert P Bartók, Mike C Payne, Risi Kondor, and Gábor Csányi. Gaussian approximation potentials: The accuracy of quantum mechanics, without the electrons. *Phys. Rev. Lett.*, 104(13):136403, 2010.
- ⁶ Jonathan Vandermause, Steven B Torrisi, Simon Batzner, Yu Xie, Lixin Sun, Alexie M Kolpak, and Boris Kozinsky. On-the-fly active learning of interpretable bayesian force fields for atomistic rare events. *npj Comput. Mater.*, 6(1):1–11, 2020.
- ⁷ Simon Batzner, Albert Musaelian, Lixin Sun, Mario Geiger, Jonathan P Mailoa, Mordechai Kornbluth, Nicola Molinari, Tess E Smidt, and Boris Kozinsky. E (3)-equivariant graph neural networks for data-efficient and accurate interatomic potentials. *Nat. Commun.*, 13(1):2453, 2022.
- ⁸ Chi Chen, Weike Ye, Yunxing Zuo, Chen Zheng, and Shyue Ping Ong. Graph networks as a universal machine learning framework for molecules and crystals. *Chem. Mater.*, 31(9):3564–3572, 2019.
- ⁹ Chi Chen and Shyue Ping Ong. A universal graph deep learning interatomic potential for the periodic table. *Nat. Comput. Sci.*, 2(11):718–728, 2022.
- ¹⁰ Ryosuke Jinnouchi, Jonathan Lahnsteiner, Ferenc Karsai, Georg Kresse, and Menno Bokdam. Phase transitions of hybrid perovskites simulated by machine-learning force fields trained on the fly with bayesian inference. *Phys. Rev. Lett.*, 122(22):225701, 2019.
- ¹¹ Ryosuke Jinnouchi, Ferenc Karsai, and Georg Kresse. On-the-fly machine learning force field generation: Application to melting points. *Phys. Rev. B*, 100(1):014105, 2019.
- ¹² Zhenwei Li, James R Kermode, and Alessandro De Vita. Molecular dynamics with on-the-fly machine learning of quantum-mechanical forces. *Phys. Rev. Lett.*, 114(9):096405, 2015.
- ¹³ Evgeny V Podryabinkin and Alexander V Shapeev. Active learning of linearly parametrized interatomic potentials. *Comput. Mater. Sci.*, 140:171–180, 2017.
- ¹⁴ M Hodapp and A Shapeev. In operando active learning of interatomic interaction during large-scale simulations. *Mach. Learn.: Sci. Technol.*, 1(4):045005, sep 2020.
- ¹⁵ Tom Young, Tristan Johnston-Wood, Volker L. Deringer, and Fernanda Duarte. A transferable active-learning strategy for reactive molecular force fields. *Chem. Sci.*, pages –, 2021.

- ¹⁶ Aldo Glielmo, Claudio Zeni, and Alessandro De Vita. Efficient nonparametric n-body force fields from machine learning. Phys. Rev. B, 97(18):184307, 2018.
- ¹⁷ Aldo Glielmo, Claudio Zeni,  Fekete, and Alessandro De Vita. Building nonparametric n-body force fields using gaussian process regression. In Machine Learning Meets Quantum Physics, pages 67–98. Springer, 2020.
- ¹⁸ Yu Xie, Jonathan Vandermause, Lixin Sun, Andrea Cepellotti, and Boris Kozinsky. Bayesian force fields from active learning for simulation of inter-dimensional transformation of stanene. npj Comput. Mater., 7(1):1–10, 2021.
- ¹⁹ Jonathan Vandermause, Yu Xie, Jin Soo Lim, Cameron J. Owen, and Boris Kozinsky. Active learning of reactive bayesian force fields: Application to heterogeneous hydrogen-platinum catalysis dynamics, 2021.
- ²⁰ Ralf Drautz. Atomic cluster expansion for accurate and transferable interatomic potentials. Phys. Rev. B, 99(1), January 2019.
- ²¹ Steve Plimpton. Fast parallel algorithms for short-range molecular dynamics. J. Comput. Phys., 117(1):1–19, 1995.
- ²² Donghoon Kim, Ray F Smith, Ian Karl Ocampo, Federica Coppari, Michelle C Marshall, MK Ginnane, June K Wicks, Sally June Tracy, M Millot, A Lazicki, et al. Structure and density of silicon carbide to 1.5 tpa and implications for extrasolar planets. Nat. Commun., 13(1):1–9, 2022.
- ²³ Nikku Madhusudhan, Kanani KM Lee, and Olivier Mousis. A possible carbon-rich interior in super-earth 55 cancri e. Astrophys. J. Lett., 759(2):L40, 2012.
- ²⁴ AK Speck, MJ Barlow, and CJ Skinner. The nature of the silicon carbide in carbon star outflows. Mon. Notices Royal Astron. Soc., 288(2):431–456, 1997.
- ²⁵ SJ Tracy, RF Smith, JK Wicks, DE Fratanduono, AE Gleason, CA Bolme, VB Prakapenka, S Speziale, Karen Appel, A Fernandez-Paella, et al. In situ observation of a phase transition in silicon carbide under shock compression using pulsed x-ray diffraction. Phys. Rev. B, 99(21):214106, 2019.
- ²⁶ T Sekine and T Kobayashi. Shock compression of 6h polytype sic to 160 gpa. Phys. Rev. B, 55(13):8034, 1997.
- ²⁷ TJ Vogler, WD Reinhart, LC Chhabildas, and DP Dandekar. Hugoniot and strength behavior of silicon carbide. J. Appl. Phys., 99(2):023512, 2006.

- ²⁸ Francesca Miozzi, Guillaume Morard, Daniele Antonangeli, Alisha N Clark, Mohamed Mezouar, Caroline Dorn, A Rozel, and Guillaume Fiquet. Equation of state of sic at extreme conditions: New insight into the interior of carbon-rich exoplanets. J. Geophys. Res. Planets, 123(9):2295–2309, 2018.
- ²⁹ Minoru Yoshida, Akifumi Onodera, Masaki Ueno, Kenichi Takemura, and Osamu Shimomura. Pressure-induced phase transition in sic. Phys. Rev. B, 48(14):10587, 1993.
- ³⁰ Yuto Kidokoro, Koichiro Umemoto, Kei Hirose, and Yasuo Ohishi. Phase transition in sic from zinc-blende to rock-salt structure and implications for carbon-rich extrasolar planets. Am. Mineral., 102(11):2230–2234, 2017.
- ³¹ Kierstin Daviau and Kanani KM Lee. Zinc-blende to rocksalt transition in sic in a laser-heated diamond-anvil cell. Phys. Rev. B, 95(13):134108, 2017.
- ³² Cheng-Zhang Wang, Rici Yu, and Henry Krakauer. Pressure dependence of born effective charges, dielectric constant, and lattice dynamics in sic. Phys. Rev. B, 53(9):5430, 1996.
- ³³ Zheng Ran, Chunming Zou, Zunjie Wei, Hongwei Wang, Rong Zhang, and Ning Fang. Phase transitions and elastic anisotropies of sic polymorphs under high pressure. Ceram. Int., 47(5):6187–6200, 2021.
- ³⁴ WH Lee and XH Yao. First principle investigation of phase transition and thermodynamic properties of sic. Comput. Mater. Sci., 106:76–82, 2015.
- ³⁵ Murat Durandurdu. Pressure-induced phase transition of sic. J. Phys. Condens. Matter, 16(25):4411, 2004.
- ³⁶ Yu-Ping Lu, Duan-Wei He, Jun Zhu, and Xiang-Dong Yang. First-principles study of pressure-induced phase transition in silicon carbide. Physica B Condens. Matter, 403(19-20):3543–3546, 2008.
- ³⁷ HY Xiao, Fei Gao, Xiaotao T Zu, and William J Weber. Ab initio molecular dynamics simulation of a pressure induced zinc blende to rocksalt phase transition in sic. J. Phys. Condens. Matter, 21(24):245801, 2009.
- ³⁸ S Gorai, C Bhattacharya, and G Kondayya. Pressure induced structural phase transition in sic. In AIP Conf Proc, volume 1832, page 030010. AIP Publishing LLC, 2017.
- ³⁹ Tavneet Kaur and MM Sinha. First principle study of structural, electronic and vibrational properties of 3c-sic. In AIP Conf Proc, volume 2265, page 030384. AIP Publishing LLC, 2020.
- ⁴⁰ J. Tersoff. Chemical order in amorphous silicon carbide. Phys. Rev. B, 49(23):16349, 1994.

- ⁴¹ Paul Erhart and Karsten Albe. Analytical potential for atomistic simulations of silicon, carbon, and silicon carbide. Phys. Rev. B, 71(3), January 2005.
- ⁴² Fuyuki Shimojo, Ingvar Ebbsjö, Rajiv K Kalia, Aiichiro Nakano, Jose P Rino, and Priya Vashishta. Molecular dynamics simulation of structural transformation in silicon carbide under pressure. Phys. Rev. Lett., 84(15):3338, 2000.
- ⁴³ Priya Vashishta, Rajiv K. Kalia, Aiichiro Nakano, and José Pedro Rino. Interaction potential for silicon carbide: A molecular dynamics study of elastic constants and vibrational density of states for crystalline and amorphous silicon carbide. J. Appl. Phys., 101(10):103515, May 2007.
- ⁴⁴ Kyung-Han Kang, Taihee Eun, Myong-Chul Jun, and Byeong-Joo Lee. Governing factors for the formation of 4h or 6h-SiC polytype during SiC crystal growth: An atomistic computational approach. J. Cryst. Growth, 389:120–133, March 2014.
- ⁴⁵ Fei Gao and William J. Weber. Empirical potential approach for defect properties in 3c-SiC. Nucl. Instrum. Methods Phys. Res. B, 191(1-4):504–508, 2002.
- ⁴⁶ Chris M Handley, Glenn I Hawe, Douglas B Kell, and Paul LA Popelier. Optimal construction of a fast and accurate polarisable water potential based on multipole moments trained by machine learning. Phys. Chem. Chem. Phys., 11(30):6365–6376, 2009.
- ⁴⁷ Albert P Bartók, James Kermode, Noam Bernstein, and Gábor Csányi. Machine learning a general-purpose interatomic potential for silicon. Phys. Rev. X, 8(4):041048, 2018.
- ⁴⁸ Linfeng Zhang, Jiequn Han, Han Wang, Roberto Car, and E Weinan. Deep potential molecular dynamics: a scalable model with the accuracy of quantum mechanics. Phys. Rev. Lett., 120(14):143001, 2018.
- ⁴⁹ Albert Musaelian, Simon Batzner, Anders Johansson, Lixin Sun, Cameron J. Owen, Mordechai Kornbluth, and Boris Kozinsky. Learning local equivariant representations for large-scale atomistic dynamics. Nat. Commun., 14(1):579, February 2023.
- ⁵⁰ Jonathan P Mailoa, Mordechai Kornbluth, Simon Batzner, Georgy Samsonidze, Stephen T Lam, Jonathan Vandermause, Chris Ablitt, Nicola Molinari, and Boris Kozinsky. A fast neural network approach for direct covariant forces prediction in complex multi-element extended systems. Nat. Mach. Intell., 1(10):471–479, 2019.
- ⁵¹ Wei Chen and Liang-Sheng Li. The study of the optical phonon frequency of 3c-sic by molecular dynamics simulations with deep neural network potential. J. Appl. Phys., 129(24):244104, 2021.

- ⁵² Baoqin Fu, Yandong Sun, Linfeng Zhang, Han Wang, and Ben Xu. Deep learning inter-atomic potential for thermal and phonon behaviour of silicon carbide with quantum accuracy. arXiv preprint arXiv:2110.10843, 2021.
- ⁵³ Senja Ramakers, Anika Maruszczyk, Maximilian Amsler, Thomas Eckl, Matous Mrovec, Thomas Hammerschmidt, and Ralf Drautz. Effects of thermal, elastic, and surface properties on the stability of sic polytypes. Phys. Rev. B, 106:075201, Aug 2022.
- ⁵⁴ Federico A Soria, Weiwei Zhang, Patricia A Paredes-Olivera, Adri CT Van Duin, and Eduardo M Patrito. Si/c/h reaxff reactive potential for silicon surfaces grafted with organic molecules. J. Phys. Chem. C, 122(41):23515–23527, 2018.
- ⁵⁵ Yu Xie, Jonathan Vandermause, Senja Ramakers, Nakib H. Protik, Anders Johansson, and Boris Kozinsky. Supplementary materials. 2022.
- ⁵⁶ G Lucas, M Bertolus, and L Pizzagalli. An environment-dependent interatomic potential for silicon carbide: calculation of bulk properties, high-pressure phases, point and extended defects, and amorphous structures. J. Phys. Condens. Matter, 22(3):035802, 2009.
- ⁵⁷ Peter Mahler Larsen, Søren Schmidt, and Jakob Schiøtz. Robust structural identification via polyhedral template matching. Model. Simul. Mater. Sci. Eng., 24(5):055007, 2016.
- ⁵⁸ Alexander Stukowski. Visualization and analysis of atomistic simulation data with ovito—the open visualization tool. Model. Simul. Mater. Sci. Eng., 18(1):015012, 2009.
- ⁵⁹ A Togo and I Tanaka. First principles phonon calculations in materials science. Scr. Mater., 108:1–5, Nov 2015.
- ⁶⁰ Stanislaw Nowak. Crystal lattice dynamics of various silicon-carbide polytypes. In International Conference on Solid State Crystals 2000: Growth, Characterization, and Applications of Single Crystals, volume 4412, pages 181–186. International Society for Optics and Photonics, 2001.
- ⁶¹ D. W. Feldman, James H. Parker, W. J. Choyke, and Lyle Patrick. Phonon Dispersion Curves by Raman Scattering in SiC, Polytypes 3C, 4H, 6H, 15R, and 21R. Phys. Rev., 173(3):787–793, September 1968.
- ⁶² Shin-ichi Nakashima, Atsuo Wada, and Zenzaburo Inoue. Raman scattering from anisotropic phonon modes in sic polytypes. J. Phys. Soc. Japan, 56(9):3375–3380, 1987.
- ⁶³ J Serrano, J Stremper, M Cardona, M Schwoerer-Böhning, H Requardt, M Lorenzen, B Stojetz, P Pavone, and WJ Choyke. Determination of the phonon dispersion of zinc blende (3c) silicon carbide by inelastic x-ray scattering. Appl. Phys. Lett., 80(23):4360–4362, 2002.

- ⁶⁴ Robert M Pick, Morrel H Cohen, and Richard M Martin. Microscopic theory of force constants in the adiabatic approximation. Phys. Rev. B, 1(2):910, 1970.
- ⁶⁵ Nakib Haider Protik, Ankita Katre, Lucas Lindsay, Jesús Carrete, Natalio Mingo, and David Broido. Phonon thermal transport in 2h, 4h and 6h silicon carbide from first principles. Mater. Today Phys., 1:31–38, June 2017.
- ⁶⁶ Atsushi Togo, Laurent Chaput, and Isao Tanaka. Distributions of phonon lifetimes in brillouin zones. Phys. Rev. B, 91:094306, Mar 2015.
- ⁶⁷ Andrea Cepellotti, Jennifer Coulter, Anders Johansson, Natalya S Fedorova, and Boris Kozinsky. Phoebe: a high-performance framework for solving phonon and electron boltzmann transport equations. J. Phys. Chem. Mater., 5(3):035003, 2022.
- ⁶⁸ M Omini and A Sparavigna. An iterative approach to the phonon boltzmann equation in the theory of thermal conductivity. Physica B Condens. Matter, 212(2):101–112, 1995.
- ⁶⁹ RE Taylor, H Groot, and J Ferrier. In Thermophysical properties of CVD SiC, School of Mechanical Engineering, Purdue University, 1993.
- ⁷⁰ DJ Senior, DJ Trimble, GE Youngblood, GA Newsome, CE Moore, and JJ Woods. Effects of neutron irradiation on thermal conductivity of sic-based composites and monolithic ceramics. Fusion Sci. Technol., 30(3P2A):943–955, 1996.
- ⁷¹ D Morelli, J Heremans, C Beetz, WS Woo, G Harris, and C Taylor. Carrier concentration dependence of the thermal conductivity of silicon carbide. In Institute of Physics Conference Series, volume 137, pages 313–316. Bristol [England]; Boston: Adam Hilger, Ltd., c1985-, 1994.
- ⁷² JE Graebner, H Altmann, NM Balzaretti, R Campbell, H-B Chae, A Degiovanni, R Enck, A Feldman, D Fournier, J Fricke, et al. Report on a second round robin measurement of the thermal conductivity of cvd diamond. Diam. Relat. Mater., 7(11-12):1589–1604, 1998.
- ⁷³ Joaquin Quinonero-Candela and Carl Edward Rasmussen. A unifying view of sparse approximate gaussian process regression. J. Mach. Learn. Res., 6:1939–1959, 2005.

Uncertainty-aware Molecular Dynamics from Bayesian Active Learning for Phase Transformations and Thermal Transport in SiC

Yu Xie,^{1,*} Jonathan Vandermause,^{1,2} Senja Ramakers,^{3,4}
Nakib H. Protik,¹ Anders Johansson,¹ and Boris Kozinsky^{1,5,†}

¹*John A. Paulson School of Engineering and Applied Sciences, Harvard University*

²*Department of Physics, Harvard University*

³*Corporate Sector Research and Advance Engineering, Robert Bosch GmbH, Renningen*

⁴*Interdisciplinary Centre for Advanced Materials Simulation, Ruhr-Universität Bochum*

⁵*Robert Bosch LLC, Research and Technology Center*

Supplementary Materials

Supplementary Methods	2
Supplementary Method 1: Select Uncertainty Threshold by Training Set Uncertainty	2
Supplementary Tables	3
Supplementary Table 1: On-the-fly Training Settings	3
Supplementary Table 2: Training Set Collected from Bayesian Active Learning	4
Supplementary Table 3: Elasticity	5
Supplementary Table 4: Performance Comparison	6
Supplementary Figures	7
Supplementary Figure 1: Variance Correlations	7
Supplementary Figure 2: Polytype Stability	8
Supplementary Figure 3: Phonon Dispersion from Models with Different Cutoffs	9
Supplementary Figure 4: Non Analytic Correction on the Thermal Conductivity	10
Supplementary Figure 5: Accuracy Comparison of 2+3-body and ACE-based Models	11
Supplementary References	12

* xiey@g.harvard.edu

† bkoz@seas.harvard.edu

SUPPLEMENTARY METHODS

Supplementary Method 1: Select Uncertainty Threshold by Training Set Uncertainty

In the active learning, the Bayesian force field predicts uncertainty to quantify the confidence of the model of the current frame. Then the uncertainty is compared to an acquisition threshold. If the uncertainty is higher than the threshold then a DFT call is made to compute the “ground truth” energy (e), forces (f) and stress (s) of the current configuration. The uncertainties of total potential energy, forces and stress are computed from the square root of the variance of the full GP:

$$V_{pp}(\rho) = k_{pp} - \mathbf{k}_{pF}^\top (\mathbf{K}_{FF} + \mathbf{\Lambda})^{-1} \mathbf{k}_{Fp}, \quad p = e, f, s \quad (1)$$

which depend on the signal variance of the kernel function and the noise parameters σ_n . Therefore, choosing an absolute (constant) threshold throughout the active learning ignores the dependence and may determine a frame as “familiar/unfamiliar” inaccurately. In Ref.[1, 2], a multiple of σ_n is used as the threshold, such that the threshold changes while the noise parameter is optimized to a different value. In Ref.[3], a simple form of the raw uncertainty of sparse GP is used

$$V(\rho) = \frac{1}{\sigma^2} (k_{\varepsilon\varepsilon} - \mathbf{k}_{\varepsilon S} K_{SS}^{-1} \mathbf{k}_{S\varepsilon}) \quad (2)$$

where the normalization by the signal variance σ make $V(\rho)$ independent of the signal variance and noise. Then an absolute (constant) threshold can be used in this special case.

In this work, we introduce a more general way to determine the threshold. Particularly, we compute the average uncertainty \bar{V}_{train} of all the training data, and then use a multiple of \bar{V}_{train} as a threshold. In the active learning of SiC, we call the DFT when $\sqrt{\bar{V}} > 1.5\sqrt{\bar{V}_{\text{train}}}$. The relative uncertainty plotted in the Fig.2a in main text is $\sqrt{\bar{V}/\bar{V}_{\text{train}}}$.

SUPPLEMENTARY TABLES

Supplementary Table 1: On-the-fly Training Settings

Parameter	Value	Description
cutoff (\AA)	5.0	Cutoff radius of the local environment for ACE descriptors
$\sigma^{(\text{B1})}$	78.2991	Signal variance of kernel of B1 descriptors
$\sigma^{(\text{B2})}$	3.5271	Signal variance of kernel of B2 descriptors
$\sigma_{\text{n}}^{(\text{energy})}$	0.1086	Noise parameter for total energy
$\sigma_{\text{n}}^{(\text{forces})}$	0.0895	Noise parameter for forces
$\sigma_{\text{n}}^{(\text{stress})}$	0.0021	Noise parameter for stress
$n_{\text{max}}^{(\text{B1})}$	11	Maximal index of radial basis function of ACE B1 descriptors
$n_{\text{max}}^{(\text{B2})}$	8	Maximal index of radial basis function of ACE B2 descriptors
$l_{\text{max}}^{(\text{B2})}$	4	Maximal index of spherical harmonics function of ACE B2 descriptors

Table S1: For the details of the parameters of the kernels, we direct the reader to Ref.[3].
 For the details of the parameters of the ACE descriptors, we direct the reader to Ref.[4]

Supplementary Table 2: Training Set Collected from Bayesian Active Learning

System	Pressure	Temperature	τ_{sim}	τ_{wall}	N_{nodes}	N_{atoms}	N_{struc}	N_{envs}	N_{sparse}	N_{labels}
3C	0-480	2000	0.85	20.94	1	64	110	7040	550	21890
2H	0-480	2000	0.85	34.94	1	72	125	9000	625	27875
4H	0-480	2000	0.85	36.87	1	72	131	9432	655	29213
6H	0-480	2000	0.85	74.04	1	108	122	13176	610	40382
3C	0-800	300	0.85	9.78	1	64	72	4608	360	14328
RS	200-0	2000	0.55	17.22	1	64	120	7680	600	23880
Total	-	-	-	193.79	-	-	680	50936	3400	157568

Table S2: Summary of on-the-fly training for the SiC system: the simulation temperature T (K); the pressure (GPa) range of the simulation; the total simulation time τ_{sim} (ns); the total wall time of the simulation τ_{wall} (hr); the number of CPU nodes used for the training (with 32 CPUs per node); the number of atoms in the simulation N_{atoms} ; the total number of structures added to the training set N_{struc} ; the total number of local environments in all training structures N_{envs} ; the total number of local environments added to the sparse set N_{sparse} ; and the total number of training labels N_{labels} .

We note that since each on-the-fly training only uses a single CPU node with 32 cores, in practice we run these on-the-fly training simulations simultaneously on a cluster. The ‘‘System’’ in the table specifies the initial polytype/phase of the simulation. The simulations starting with 3C/2H/4H/6H are compressive with increasing pressures. The simulation starting with RS is decompressive with decreasing pressures. The pressure range in the table also specifies the compression/decompression. For example, ‘‘0-480’’ means a compressive simulation from 0 to 480 GPa, and ‘‘200-0’’ means a decompressive simulation from 200 to 0 GPa.

Supplementary Table 3: Elasticity

Polytype	Method	C_{11}	C_{33}	C_{12}	C_{13}	C_{44}	C_{66}	B_V	G_V
	EXP	390 ^a ; 395 ^e ; 371 ^c		142 ^a ; 123 ^e ; 146 ^c		150 ^b ; 256 ^a ; 236 ^e ; 111 ^c			
	DFT	384.3	384.3	127.9	127.9	239.9	239.9	213.6	195.4
3C	FLARE BFF	373.1	373.1	128.0	128.0	230.3	230.3	209.7	187.2
	Tersoff	426	426	109.9	109.9	252.7	252.7	215.3	214.8
	MEAM	402.2	402.2	115.6	115.6	215.1	215.1	211.1	186.4
	EXP								
	DFT	494.3	533.5	102.1	50.7	151.3	196.1	214.3	187.6
2H	FLARE BFF	482.8	527.2	101.0	52.7	158.1	190.9	211.7	187.2
	Tersoff	502.2	541.6	84.4	42.3	188.8	208.9	209.3	215.9
	MEAM	467.4	497.9	98.2	67.7	167.2	184.6	211.1	189.1
	EXP	501 ^d	553 ^d	111 ^d	52 ^d	163 ^d			
	DFT	487.8	533.4	105	51.9	157.9	191.4	214	188.1
4H	FLARE BFF	476.0	514.9	104.8	55.0	158.4	185.6	210.7	184.0
	Tersoff	506.6	547.7	86.6	44.9	189.1	210	212.7	216.9
	MEAM	467.2	497.9	98.4	67.7	167.2	184.4	211.1	189.1
	EXP	501 ^d	553 ^d	112 ^d	52 ^d	163 ^d			
	DFT	485.2	534.1	106	52.3	160.1	189.6	213	188.2
6H	FLARE BFF	472.2	515.3	106.1	55.3	158.4	183.1	210.3	182.8
	Tersoff	507.2	548.6	87	45.3	189.1	210.1	213.1	217
	MEAM	467.2	497.9	98.4	67.7	167.2	184.4	211.1	189

^a Ref. [5] ^b Ref. [6] ^c Ref. [7] ^d Ref. [8] ^e Ref. [9] (Unit: GPa)

Table S3: Elastic tensor ($C_{11} \sim C_{66}$), bulk modulus (B_V) and shear modulus (G_V) from experiments (EXP), DFT[10], FLARE BFF and empirical potentials (Tersoff, MEAM).

We note that since FLARE BFF is trained on DFT data but not the experiments, we expect it to give predictions closer to DFT than experiments, while as shown in Table S3, we still find good match for the four polytypes between FLARE BFF and experimental results.

Supplementary Table 4: Performance Comparison

Model	Parameters	Speed (potential)	Speed (variance)	Force MAE
2+3 body	2-body: $r_{\text{cut}} = 5\text{\AA}$, $n_{\text{grid}} = 32$ 3-body: $r_{\text{cut}} = 5\text{\AA}$, $n_{\text{grid}} = 16^3$	0.20525	$O(N_{\text{ranks}} t_{\text{potential}}^{(2+3)})$	136.5
ACE-based	$r_{\text{cut}} = 5\text{\AA}$, $n_{\text{max}} = 8$, $l_{\text{max}} = 3$	0.21123	$O(t_{\text{potential}}^{(\text{ace})})$	68.4

Table S4: Performance test with MGP potentials of SiC. Speed unit: ms · CPU/(atom · timestep). Force MAE unit: meV/Å.

2+3 body based mapped GP is an approximation, whose accuracy depends on the grid resolution of the spline interpolation, and the ranks from PCA (for variance). ACE based mapped GP is exact, which only differs from the original Sparse GP model by floating point errors. To reduce computational cost, we chose to use the $\xi = 2$ potential and $\xi = 1$ variance, where the $\xi = 1$ variance is a good approximation of the $\xi = 2$ variance, as shown in the Supplementary Information Figure S1.

The comparison of the performance between 2+3 body based MGP force field and the ACE based MGP is shown in the Table 4. The computational cost of the mapped variance of the 2+3 body based model is dominated by the PCA decomposed 3-body variance $O(N_{\text{ranks}} t_{\text{potential}}^{(2+3)})$. The computational cost of the mapped force field is $t_{\text{potential}}^{(\text{ace})} \sim O(n_{\text{descriptor}}^{\xi})$, and that of the mapped variance of ACE based model is $O(n_{\text{descriptor}}^{2\xi})$, where the ξ is the power of the kernel. Since we use $\xi = 1$ for variance and $\xi = 2$ for the force field, the cost of variance is comparable to the force field $O(t_{\text{potential}}^{(\text{ace})})$.

SUPPLEMENTARY FIGURES

Supplementary Figure 1: Variance Correlations

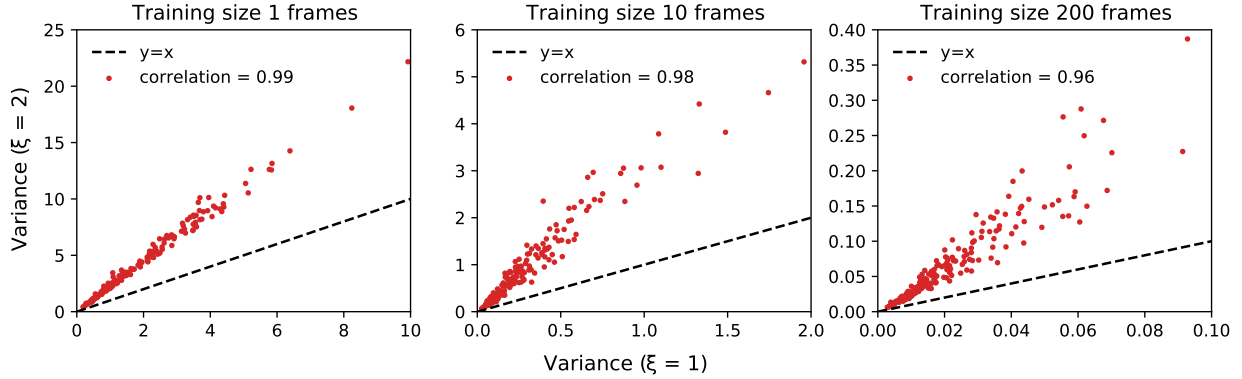


Figure S1: Variance comparison between different powers.

For the computational efficiency, we map the variance with power $\xi = 1$ of the normalized inner product kernel of sparse GP for prediction in LAMMPS. While the energy, forces and stress are predicted from power $\xi = 2$ kernel, the variance with $\xi = 1$ is an approximation of the variance from $\xi = 2$ kernel. We test the correlation between the two variances for the same testing configurations with different training set sizes. As shown in Fig.S1, the two variances have a high correlation above 90%, even though the values present a constant ratio. From Supplementary Method, we compare the uncertainty of testing data with the average training set uncertainty in the active learning. Therefore, the constant ratio does not make much difference as long as the approximate uncertainty preserves the order of high/low uncertainties.

Supplementary Figure 2: Polytype Stability

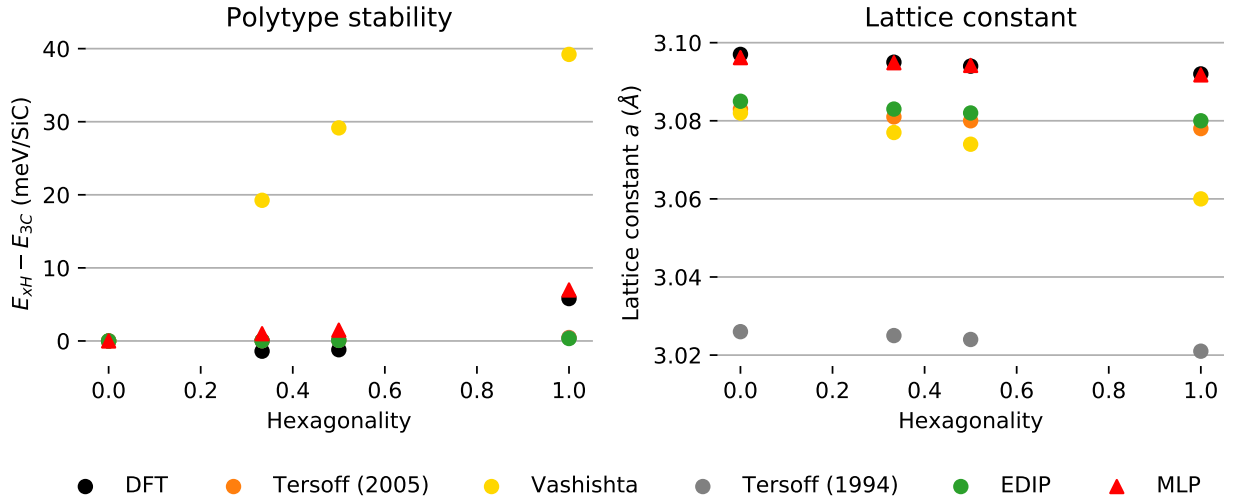


Figure S2: Polytype stability and lattice constant of 3C (hexagonality=0), 6H (hexagonality=1/3), 4H (hexagonality=1/2) and 2H (hexagonality=1), predicted from DFT, FLARE BFF and empirical potentials including Tersoff[11, 12], Vashishta[13] and EDIP[14].

We compare FLARE BFF with DFT and empirical potentials on the polytype stability and lattice constant at zero pressure. Specifically, we compute ground state energy per Si-C pair and compare the energy differences between hexagonal polytypes (2H, 4H and 6H) with the cubic one (3C). While the DFT energy differences between 4H, 6H and 3C are as small as ~ 1 meV, 2H is significantly more unstable than the other polytypes by ~ 6 meV. As shown in Fig.S2a, empirical methods such as Tersoff[11, 12] and EDIP[14] do not distinguish the energy differences between different polytypes, and Vashishta[13] potential predicts very large differences which over-stabilizes the cubic type, while the FLARE BFF reaches around 1 meV error with DFT and gives the correct polytype stability. The lattice constants of different polytypes are also compared in Fig.S2b, where the discrepancy between FLARE BFF and DFT is around 0.002\AA . And all methods manage to predict the decreasing trend while the hexagonality increases.

Supplementary Figure 3: Phonon Dispersion from Models with Different Cutoffs

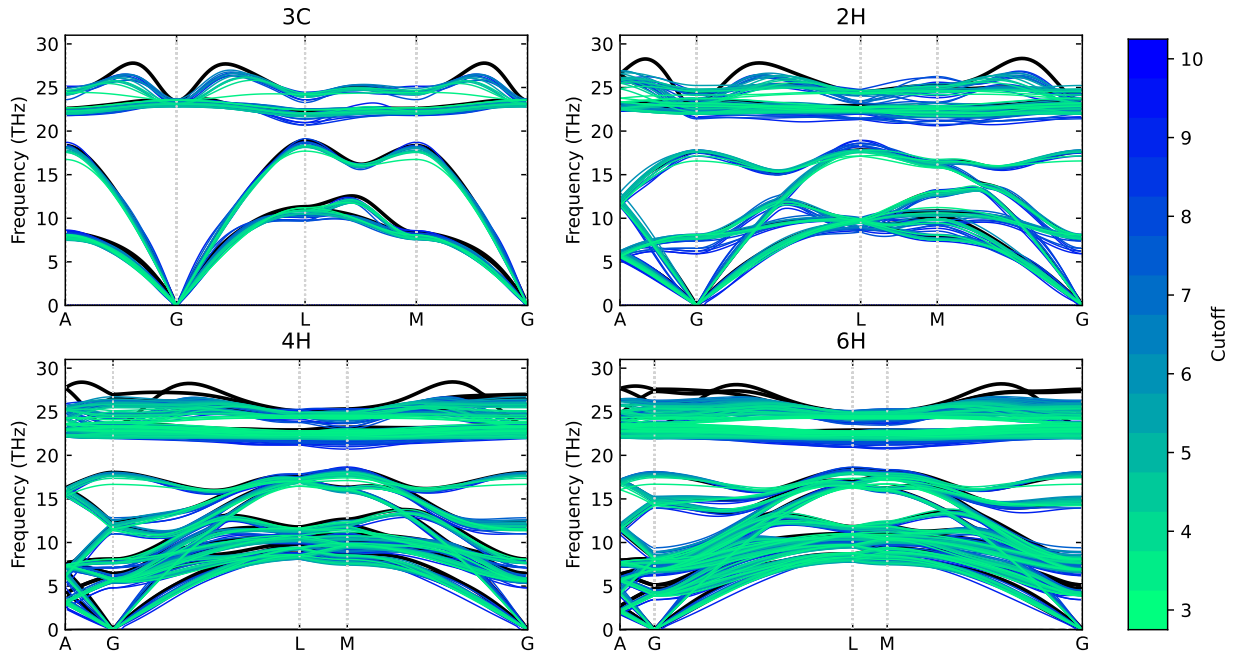


Figure S3

As shown in Fig.5 of the main text, the FLARE BFF and DFT phonon dispersions have an excellent agreement in the acoustic and transverse optical (TO) branches, but show mismatch in the longitudinal optical (LO) branches. Considering the LO-TO splitting, even though we do not include non-analytical correction, it is still likely that the polarization makes a non-trivial contribution and is not captured due to the near-sightedness of our machine learning model. Therefore, we tested how the model cutoff affects the phonon. We trained the model with cutoff from 3 to 10Å, and the phonons predicted by the models are plotted from light to dark colors. As shown in Fig.S3, all models have an excellent agreement with DFT in acoustic and TO branches, even with a cutoff as short as 3Å. While in the LO branches, the models with smaller cutoffs predict significantly flatter bands than the ones with larger cutoffs. Though with the largest cutoff our FLARE BFF still does not predict the LO branches perfectly, this result shows an evidence that one source of the mismatch in the LO branches is the long-range effect. Further investigation is needed such as introducing long-range interactions to the FLARE BFF, and will be left to our future work.

Supplementary Figure 4: Non Analytic Correction on the Thermal Conductivity

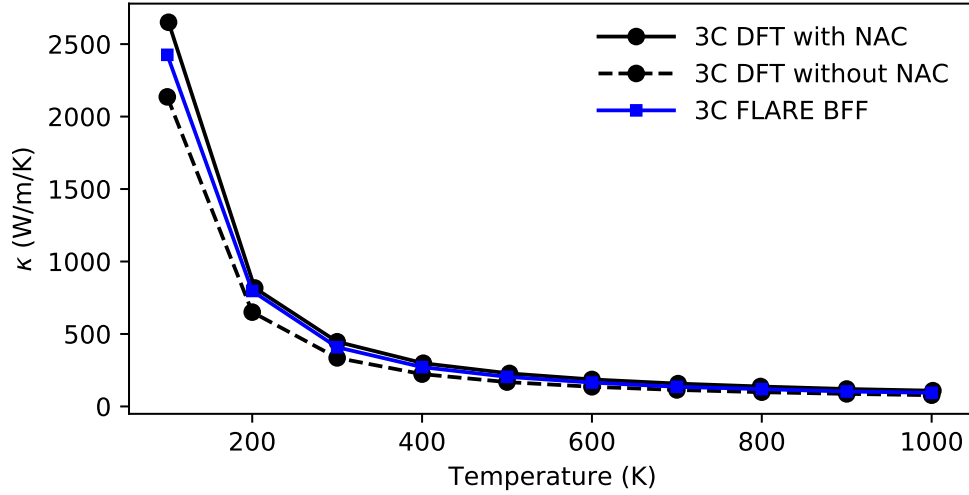


Figure S4: Thermal conductivity without and with NAC [15] at different temperatures.

We calculated the thermal conductivity from Boltzmann transport equation with the non analytical correction (NAC) term from Born effective charge, and compared it to that without NAC term at temperatures from 100 to 1000 K. Fig.S4 indicates that the exclusion of the non analytical correction term underestimates the thermal conductivity, but the underestimation is not significant. Since FLARE BFF is trained on the DFT data without long-range electrostatic interactions, and the force constants are computed without NAC term, it underestimates thermal conductivity compared to the DFT with NAC as expected.

Supplementary Figure 5: Accuracy Comparison of 2+3-body and ACE-based Models

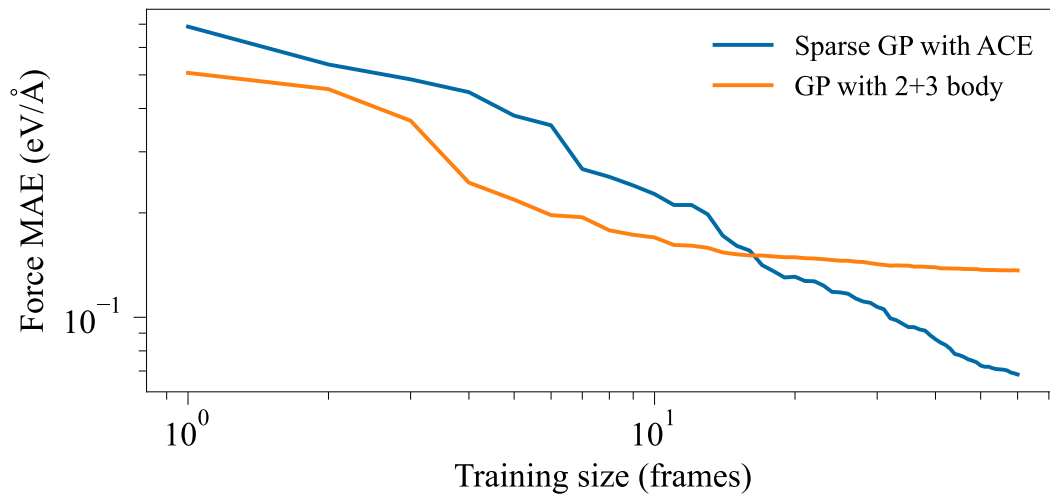


Figure S5: Comparison of accuracy between ACE-based and 2+3 body based Gaussian process force field on the bulk SiC dataset.

A comparison of accuracy between the GP model with 2+3 body descriptors and the one with ACE descriptors is made with the SiC bulk dataset, as shown in Fig.S5.

SUPPLEMENTARY REFERENCES

- [1] Vandermause, J. *et al.* On-the-fly active learning of interpretable bayesian force fields for atomistic rare events. *npj Comput. Mater.* **6**, 1–11 (2020).
- [2] Xie, Y., Vandermause, J., Sun, L., Cepellotti, A. & Kozinsky, B. Bayesian force fields from active learning for simulation of inter-dimensional transformation of stanene. *npj Comput. Mater.* **7**, 1–10 (2021).
- [3] Vandermause, J., Xie, Y., Lim, J. S., Owen, C. J. & Kozinsky, B. Active learning of reactive bayesian force fields: Application to heterogeneous hydrogen-platinum catalysis dynamics (2021). 2106.01949.
- [4] Drautz, R. Atomic cluster expansion for accurate and transferable interatomic potentials. *Phys. Rev. B* **99** (2019). URL <https://link.aps.org/doi/10.1103/PhysRevB.99.014104>.
- [5] Feldman, D. W., Parker, J. H., Choyke, W. J. & Patrick, L. Phonon Dispersion Curves by Raman Scattering in SiC, Polytypes 3C, 4H, 6H, 15R, and 21R. *Phys. Rev.* **173**, 787–793 (1968). URL <https://link.aps.org/doi/10.1103/PhysRev.173.787>.
- [6] Harrison, W. & Freeman, W. Electronic structure and the properties of solids: the physics of the chemical bond. *Journal of Molecular Structure* **71**, 355 (1981). URL <https://linkinghub.elsevier.com/retrieve/pii/0022286081851368>.
- [7] Pestka, K. A., Maynard, J. D., Gao, D. & Carraro, C. Measurement of the Elastic Constants of a Columnar SiC Thin Film. *Phys. Rev. Lett.* **100** (2008). URL <https://link.aps.org/doi/10.1103/PhysRevLett.100.055503>.
- [8] Kamitani, K. *et al.* The elastic constants of silicon carbide: A Brillouin-scattering study of 4h and 6h SiC single crystals. *J. Appl. Phys.* **82**, 3152–3154 (1997). URL <http://aip.scitation.org/doi/10.1063/1.366100>.
- [9] Djemia, P., Roussigné, Y., Dirras, G. F. & Jackson, K. M. Elastic properties of β -SiC films by Brillouin light scattering. *J. Appl. Phys.* **95**, 2324–2330 (2004). URL <http://aip.scitation.org/doi/10.1063/1.1642281>.
- [10] Ramakers, S. *et al.* Effects of thermal, elastic, and surface properties on the stability of sic polytypes. *Phys. Rev. B* **106**, 075201 (2022). URL <https://link.aps.org/doi/10.1103/>

PhysRevB.106.075201.

- [11] Erhart, P. & Albe, K. Analytical potential for atomistic simulations of silicon, carbon, and silicon carbide. *Phys. Rev. B* **71** (2005). URL <https://link.aps.org/doi/10.1103/PhysRevB.71.035211>.
- [12] Tersoff, J. Chemical order in amorphous silicon carbide. *Phys. Rev. B* **49**, 16349 (1994). URL <https://journals.aps.org/prb/abstract/10.1103/PhysRevB.49.16349>.
- [13] Vashishta, P., Kalia, R. K., Nakano, A. & Rino, J. P. Interaction potential for silicon carbide: A molecular dynamics study of elastic constants and vibrational density of states for crystalline and amorphous silicon carbide. *J. Appl. Phys.* **101**, 103515 (2007). URL <http://aip.scitation.org/doi/10.1063/1.2724570>.
- [14] Jiang, C., Morgan, D. & Szlufarska, I. Carbon tri-interstitial defect: A model for the D II center. *Phys. Rev. B* **86** (2012). URL <https://link.aps.org/doi/10.1103/PhysRevB.86.144118>.
- [15] Protik, N. H. *et al.* Phonon thermal transport in 2h, 4h and 6h silicon carbide from first principles. *Mater. Today Phys.* **1**, 31–38 (2017). URL <https://linkinghub.elsevier.com/retrieve/pii/S2542529317300743>.